Radioprotection 2024, 59(4), 296–305

https://doi.org/10.1051/radiopro/2024030

Available online at:
www.radioprotection.org

ARTICLE OPEN ACCESS

Voxel-based Monte Carlo simulation of human external exposure to terrestrial gamma radiation

A. Bouzouita[1], B. Askri[2,*], K. Manai[1] and A. Trabelsi[1,3]

[1] Faculty of Sciences of Tunis, University of Tunis El Manar, 2092 Tunis, Tunisia.
[2] Research Laboratory on Energy and Matter for Nuclear Science Development (LR16CNSTN02), National Center for Nuclear Science and Technologies, Sidi Thabet Technopark 2020, Tunis, Tunisia.
[3] National Center for Nuclear Science and Technologies, Sidi Thabet Technopark 2020, Tunis, Tunisia.

Received: 13 March 2024 / Accepted: 31 July 2024

Abstract – Organ absorbed doses are calculated for human exposure to terrestrial gamma radiation using a two-stage voxel-based Monte Carlo simulation in which the human body is represented by the voxel ICRP110 phantoms integrated in the Geant4 Monte Carlo code. The transport of photons in the soil-air medium is optimised by using a proven optimised geometry that allows tracking only those photons that have a high chance of reaching the standing reference phantom on the ground. For an optimal tracking within the voxel phantom, a nested parameterisation navigation technique implemented in Geant4 is applied. The organ-absorbed doses and the correspondent effective dose are calculated for the natural radioactive series of ^{238}U and ^{232}Th and for the ^{40}K and ^{137}Cs radionuclides. The results are compared to published studies that used the less precise mathematical based MIRD phantoms and to results derived from the ICRP144 report using the most advanced voxel phantom. The degree of agreement and the source of discrepancy between the realistic voxel model of the human body and the mathematical model used in the literature are analysed.

Keywords: voxel phantom / Monte Carlo / radioactive series / organ dose conversion factors

1 Introduction

Accurate dosimetry is essential for establishing protection standards for human exposure to radioactive pollutants. Access to radioactivity level in the soil is important to derive the effective dose received by the population. The effective dose, introduced in the International Commission on Radiological Protection publication 60 (ICRP, 1991, 2007), is the risk-related quantity in radiation protection and is defined as the weighted average of the organ equivalent doses. Organ equivalent doses must be calculated using dose conversion factors, also called DCF and expressed in nSv h^{-1} per Bq Kg^{-1}, to provide a reference to the radioactivity concentration in the soil. Given the complexity of experimentally determining DCFs, Monte Carlo simulation is a powerful tool for calculating these DCFs.

Organ DCFs for external exposure to soil radioactivity are scarce. Most literature focuses on the calculation of the effective dose (Jacob *et al.*, 1986; Saito, 1991; Eckerman and Ryman, 1993; Krstic and Nikezic, 2009, Askri *et al.*, 2023) and very few works are dedicated to the detailed calculation of organ doses (Zankl *et al.*, 1997; Sanusi *et al.*, 2021). Stylized mathematical phantoms were used in the Monte Carlo calculation of DCFs for external exposure to gamma radiation emitted from sources distributed in the ground. This includes the ORNL phantom proposed by Oak Ridge National Laboratory for modeling the human body based on analytical equations and the anthropomorphic phantom MIRD proposed by the Internal Radiation Dose Committee (Snyder *et al.*, 1978; Kramer *et al.*, 1982), which is a Series of volumes and curves created to adjust the dimensions and weight of the ICRP reference man. Although mathematical phantoms provide a good approximation of the human body, they do not reflect the actual complexity of human anatomy, which is characterized by detailed structures at various scales. Recently the International Commission on Radiological Protection (ICRP) adopted the voxel models for their computational phantoms to represent the reference computational phantoms of the human body in adult male (RCP-AM) and adult female (RCP-AF) (ICRP, 2009). The ICRP-110 reference phantoms are a set of voxel models of the human body created from patient computed tomography (CT) images and adjusted to match reference data from ICRP Publication 89 (ICRP, 2002). When compared to previous stylized mathematical phantoms (Johnson and Dunford, 1985; ICRP, 2009), these voxel

*Corresponding author: boubaker.askri@cnstn.rnrt.tn

phantoms greatly enhance the depiction of the human anatomy. Voxel-based phantoms are often used to estimate organ doses in diagnostic radiology and occupational exposures (Rezaeian *et al.*, 2022; Portugal *et al.*, 2022; Xu *et al.*, 2023). ICRP Publication 144 (ICRP, 2020) proposed a method using voxel phantoms for Monte Carlo calculation of organ DCFs in the special case of planar gamma-ray sources in soil. The Monte Carlo simulation was performed using the radiation transport code PHITS (ICRP, 2020). This calculation serves as basis for estimating organ DCFs corresponding to anthropogenic radionuclides that are distributed exponentially with soil depth. However, given the enormous computational time required to perform Monte Carlo calculations on external exposure to gamma rays from the ground using voxel phantoms, most of previous researches have focused on using simpler, mathematically based phantoms for such calculations.

Askri *et al.*, (2008) derived a geometrically optimised model for the Monte Carlo calculation of the gamma radiation field in air due to radioactive sources distributed in the soil, reducing computation time (Askri *et al.*, 2008; Askri, 2015, 2016). In addition, important advances have been made in CERN's Geant4 Monte Carlo simulation code (Agostinelli *et al.*, 2003; Allison *et al.*, 2016), which consists in the implementation of an optimised Monte Carlo algorithm for transporting particles in voxel-based geometry.

In the present work, taking advantage of these optimisation techniques, a two-stage Monte Carlo calculation simulation is proposed to estimate human organ DCFs for soil-distributed radioactive sources. In the first stage, gamma photons emitted by sources distributed in the ground are transported in the soil-air optimised geometry until reaching a cylindrical surface surrounding a standing human phantom on the ground surface. The second stage uses the ICRP110 reference computational voxel-based male and female phantoms in the Geant4 code to calculate absorbed doses in 141 organs and tissues due to photons originating from the surrounding surface. DCFs for the natural radioactive series of ^{238}U and ^{232}Th and for the ^{40}K and ^{137}Cs radionuclides are determined and compared with published results in the literature.

2 Material and methods

2.1 The ICRP110 voxel based phantom

The human computational male and female phantoms were created from a set of clinical whole-body CT images: a 38-year-old male (176 cm, 70 kg) and a 43-year-old female (163 cm, 60 kg). These were scaled to match the ICRP adult reference standards (ICRP, 2009), presenting 141 organs/tissues. Each voxel in the phantom is identified by an organ ID, arranged in data files layer by layer, line by line, and column by column, increasing along the x-, y-, and z-axes. Slice numbers increase from the toes to the top of the body, row numbers increase from front to back, and column numbers increase from right to left. The male human phantom is voxelized in *x*,*y*,*z* with $254 \times 127 \times 222$ voxels with dimensions $2{,}137 \times 2{,}137 \times 8$ mm. The female human phantom is voxelized in *x*,*y*,*z* with $299 \times 137 \times 348$ voxels with dimensions $1.775 \times 1.775 \times 4.84$ mm.

2.2 Soil-air optimised geometry

In the first stage of the Monte Carlo simulation carried out in the present work, gamma photons emitted from sources uniformly distributed in the soil are transported. This process is time-consuming due to the semi-infinite extent of the soil and air media, and the need for a large number of photons to achieve statistical accuracy. The complexity increases when particles are transported inside the phantom, requiring extensive computational time. To address these challenges, an optimised geometry for the soil is proposed, considering only photons likely to reach the exposed human phantom. This geometry is based on physical criteria, including the exponential attenuation law of gamma radiation (Askri *et al.*, 2008; Askri, 2015). Implementing this geometry significantly reduces computational time for photon transport in the soil-air medium (Askri *et al.*, 2008; Askri, 2015, 2016). For a nominal soil depth d and detection height h above the ground, the useful sources are contained in a soil volume bounded by the surface:

$$r(z) = \left((d + \hat{\mu} h)^2 \frac{(h - z)^2}{(\hat{\mu} h - z)^2} - (h - z)^2 \right)^{\frac{1}{2}} + R_d, \qquad (1)$$

where $r(z)$ is the lateral extent as function of the depth z; $\hat{\mu} = \frac{\mu_a}{\mu_s}$; μ_a the linear attenuation coefficient in the air, μ_s the linear attenuation coefficient in the soil and R_d the radius of a virtual surface detector located at the height h above the ground. As defined in Askri *et al.* (2008), the nominal depth of soil is the depth bellow which any emitted radiation is strongly attenuated before reaching the detection location. Considering the phantom dimensions, it is possible to consider the totality of the gamma radiation field reaching the phantom by taking h and R_d equal to 2 m in equation (1).

2.3 Geant4 Nested Parameterisation navigation technique

Geant4 provides various ways to describe geometry, each with a corresponding navigation technique to determine the particle's volume at each step. Traditional navigation in a voxelized human phantom is time-consuming due to high memory demands. To optimise memory use, Geant4 offers the nested parameterization navigation technique via the G4Nested class (Agostinelli *et al.*, 2003; Allison *et al.*, 2016). The G4Nested class uses parameterization, creating a single volume in memory that appears in multiple locations with different materials at runtime. This technique improves upon the G4Replica tool, which represents multiple volumes as a single volume but requires consistent shape and placement. G4Replica cannot assign different materials to copies when cutting geometry in three directions. G4Nested solves this by using G4Replica for two axes and a one-dimensional parameterization for the third axis, dividing the simulation space into intelligent voxels. Each voxel contains a limited set of geometry volumes, and a map links each volume to its smart voxel. The ComputeMaterial method of G4VNestedParameterization calculates the material for each voxel using the indices from the *x*, *y*, and *z* replicas.

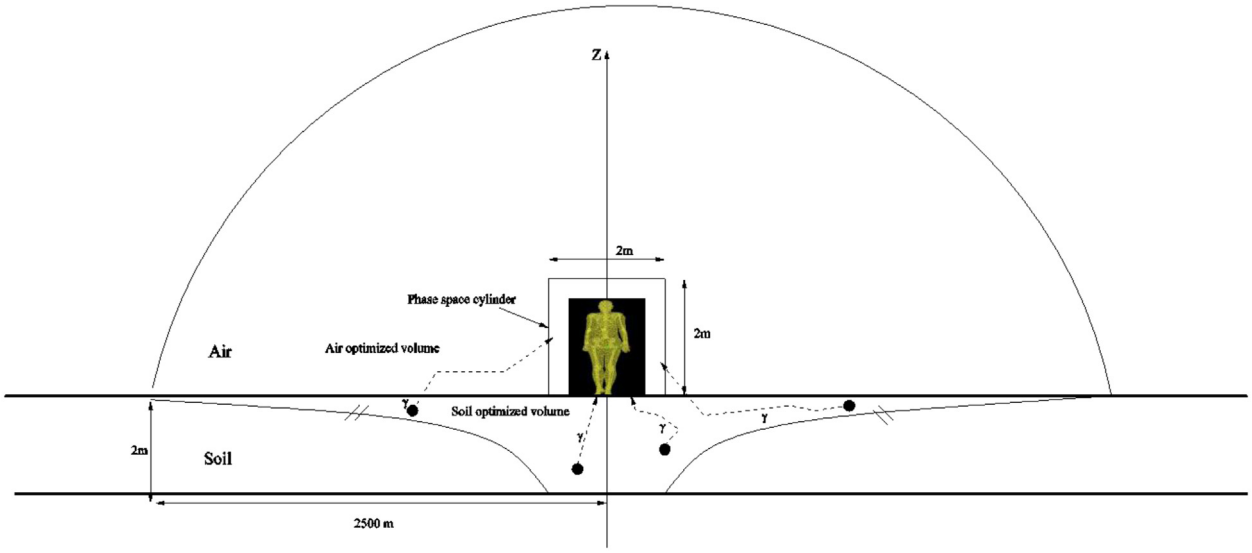

Fig. 1. Geometric setup for the Monte Carlo simulation of dose to organs conversion factors due to gamma radiation emitted from sources uniformly distributed in the ground.

2.4 Monte Carlo simulation and organ doses calculation

The first stage of the Monte Carlo simulation models the soil with optimised geometry for a depth of 2 m and a detection height of 2 m. The lateral extent of the soil is set at 2500 m, with the air modeled as a hemispherical volume with a radius of 2500 m. The simulation geometry with the standing phantom on the ground surface is depicted in Figure 1. The densities and chemical compositions of air and soil match those from Saito and Jacob (1995). The air with a density of 1.29 mg cm^{-3} is composed of 75.5% N, 23.2% O and 1.3% Ar. The soil with a density of 1.6 g cm^{-3} is composed of 57.5 % O, 2.2 % H, 26.2% Si, 8.5% Al and 5.6% Fe Gamma photons are tracked until they reach a cylinder (2 m radius, 2 m height) around the phantom. Livermore's low-energy electromagnetic models are used in Geant4, considering Compton scattering, Rayleigh scattering, pair production, and the photoelectric effect (Agostinelli *et al.*, 2003). In this stage the number of emitted photons varied from 2×10^8 to 5×10^8 photons per primary emission energy to maintain calculation accuracy within 4% uncertainty. In the second stage of the simulation, gamma photons are emitted at the cylinder's surface according to the phase space variables precalculated in the first stage. These variables consist of the energy, the three coordinates of the direction unit vector and the three cylindrical coordinates of the point of impact of the incident photon. The QGSP_BIC_HP Geant4 physics list is used, suitable for energies below 200 MeV that characterize radiation protection, shielding and medical applications (Agostinelli *et al.*, 2003; Incerti *et al.*, 2020). It includes standard Geant4 electromagnetic physics recommended for photons and charged particles interacting with biological tissues. No physical approximations are made, and particle transport occurs within the voxel-based phantom geometry. A total of 5×10^7 of photons are emitted for each primary energy of interest. Organ DCFs are calculated based on total energy deposited in the 141 organs of the ICRP110 phantom ensuring 5 % precision. Geant4.11.2.1 software on a Linux Ubuntu 20.4 system with a 12-core Intel Core i7-12700 and 32 GB RAM was used for the simulation.

Organ equivalent DCFs are identical to organ absorbed doses owing to a gamma radiation weighting factor of 1 (ICRP, 2007). The active marrow absorbed dose and the skeletal absorbed dose are determined according to the methods described in ICRP 116 (ICRP, 2010) with the absorbed dose for red bone marrow being the mass-weighted average of doses in the skeleton. The skeleton is divided into the 19 bones and bone groups for which individual data on red bone marrow content and marrow cellularity are given in Publication 70 (ICRP, 1995). This sub-division resulted in 44 different identification numbers in the skeleton: two – cortical bone and spongiosa – for each of the 19 bones (ICRP, 2010). The effective dose rate per activity concentration is calculated as a sex- averaged of the equivalent doses assessed for organ or tissue T of the Reference Male and Reference Female according to:

$$E = \sum_T w_T \left[\frac{H_T(male) + H_T(female)}{2} \right], \qquad (2)$$

where $H_T(male)$ and $H_T(female)$ are equivalent doses for tissue T in male and female phantom and w_T is the tissue weighting factor for organ T recommended in (ICRP, 2007).

Finally, to improve the language of the present work, the authors used the revision tool REF-N-WRITE version 6. The authors reviewed and edited the content as necessary after using this tool. The scientific findings and conclusions presented in this work were not produced by generative AI tools. They are the sole product of the authors' research and analysis. The authors assume full responsibility for the accuracy of the results.

3 Results and discussion

Absorbed dose conversion factors (DCF) as a function of gamma radiation energy for various organs of the female

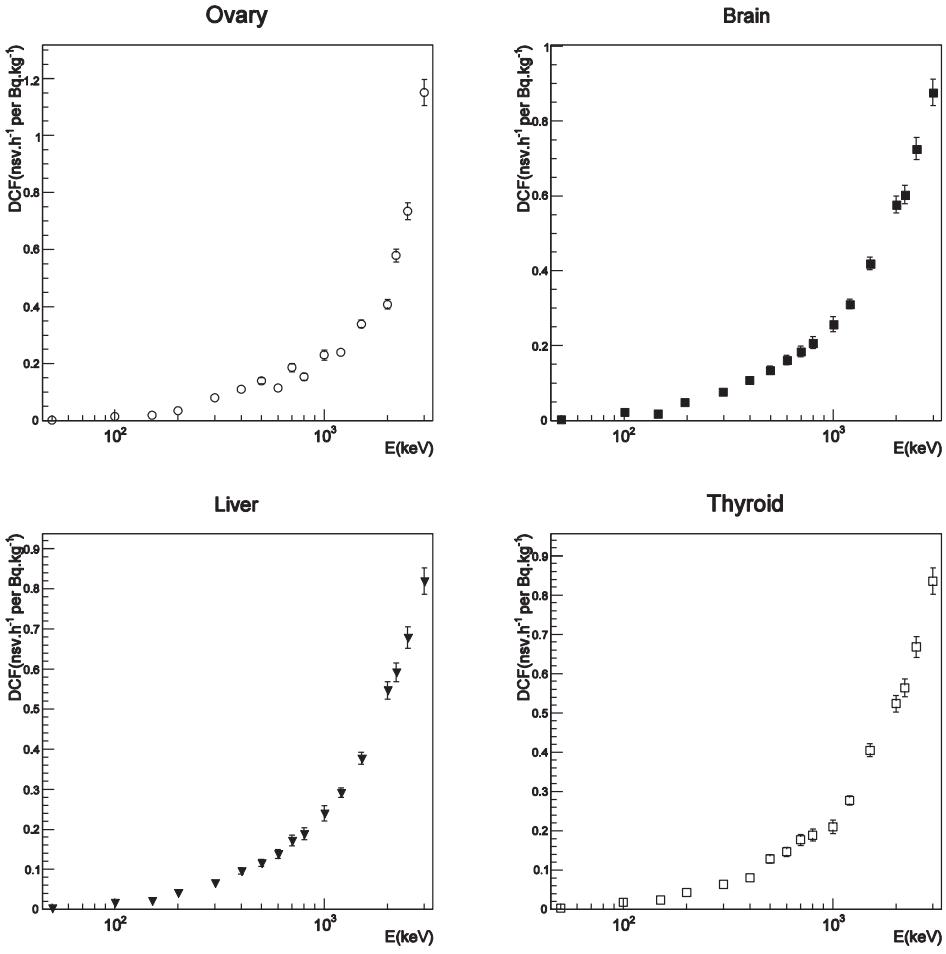

Fig. 2. Dose to organ conversion factors as function of primary gamma-ray energy for different organs of the female ICRP110 voxel phantom and for sources uniformly distributed in the ground.

ICRP110 voxel phantom and uniformly distributed soil sources are presented in Figure 2. The DCF increases with emission energy and is of a similar magnitude across different organs due to comparable shielding effects. The absorbed dose rate in various organs for the natural radioactive series of ^{238}U, ^{232}Th and the ^{40}K radionuclide as well as for the anthropogenic ^{137}Cs radionuclide are shown in Tables 1 and 2 for a female and male phantoms. Gamma ray emission energies and yields for the different series are issued from (Askri, 2015). The advantage of voxel-based Monte Carlo simulations over mathematical phantoms is evident in the detailed dose distribution information. Tables 1 and 2 indicate higher organ DCFs for the ^{232}Th series compared to the ^{238}U series, attributed to the higher gamma emission yield of ^{232}Th. The ^{137}Cs and ^{40}K radionuclides exhibit lower DCFs due to lower emission energies and decay probabilities, respectively. Skin DCFs are higher due to its large surface area and the energy loss of secondary electrons in the skin layers (Xu *et al.*, 2023; Krstic and Nikezic, 2009). Organs such as testes and breasts also show higher doses due to their protruding structure, while other organs receive comparable doses due to structural shielding.

Table 3 shows a comparison between the results of the present work and those of Sanusi *et al.* (2021), who used a single-stage Monte Carlo simulation on MCNP code with a mathematical MIRD phantom. The comparison is also done with the organ DCFs, which are obtained indirectly by multiplying the organ conversion coefficients (Sv/Gy) normalising the absorbed doses in organs to kerma free in air that were calculated by Zankl *et al.* (1997) and the absorbed dose in air conversion factors from Saito and Jacob (1995). Their calculation was performed in tow-stage Monte Carlo simulation using an early version of a MIRD mathematical phantom and the Monte Carlo YURI code (Saito and Moriuchi, 1985). Our results show higher DCFs for most organs, likely due to the more accurate voxel-based geometry, the optimised geometry of the soil-air medium and the different physical models used here. The discrepancy in red bone marrow DCFs can be attributed to the more detailed skeleton constituents considered in our voxel phantom compared to the MIRD phantom. It is worth to note that in the MIRD phantom, eight skeleton constituents are taken into account instead of 19 taken into account in the ICRP110 voxel-based phantom used in the present work (Sanusi *et al.*, 2021). A large discrepancy can also be seen for the muscle and the skin tissues. As stated by Sanusi *et al.* (2021), there is no way to mathematically represent a clear and precise muscle tissue distribution in the phantom. Therefore, for the MIRD phantom, the body volume of head, neck, trunk, and legs approximates the muscles (Sanusi *et al.*, 2021). For

Table 1. Absorbed dose in different organs of the ICRP Female phantom for the natural radioactive series and for the ^{137}Cs uniformly distributed in the ground.

Organs/tissues	DCF(nGy h^{-1} per Bq kg^{-1})			
	^{238}U	^{232}Th	^{40}K	^{137}Cs
Adrenal left	0.360	0.440	0.040	0.074
Adrenal right	0.342	0.466	0.033	0.075
Gall bladder wall	0.317	0.449	0.037	0.080
Gall bladder contents	0.344	0.460	0.041	0.087
Urinary bladder wall	0.381	0.530	0.042	0.103
Urinary bladder contents	0.371	0.528	0.043	0.099
Brain	0.386	0.523	0.044	0.103
Breast left adipose tissue	0.411	0.577	0.045	0.114
Breast left glandular tissue	0.400	0.539	0.047	0.106
Breast right adipose tissue	0.412	0.550	0.046	0.112
Breast right glandular tissue	0.378	0.521	0.040	0.102
Ascending colon wall	0.345	0.471	0.038	0.091
Ascending colon contents	0.357	0.479	0.041	0.092
Transverse colon wall right	0.343	0.478	0.036	0.090
Transverse colon contents right	0.352	0.491	0.039	0.093
Transverse colon wall left	0.350	0.494	0.040	0.097
colon contents left	0.367	0.510	0.049	0.099
Descending colon wall	0.353	0.494	0.039	0.093
Descending colon contents	0.350	0.524	0.038	0.090
Sigmoid colon wall	0.340	0.488	0.039	0.086
Sigmoid colon contents	0.361	0.503	0.044	0.092
Kidney left cortex	0.331	0.477	0.039	0.084
Kidney left medulla	0.341	0.490	0.040	0.088
Kidney left pelvis	0.335	0.484	0.036	0.078
Kidney right cortex	0.344	0.475	0.038	0.086
Kidney right medulla	0.338	0.456	0.039	0.090
Kidney right pelvis	0.320	0.428	0.032	0.090
Liver	0.353	0.481	0.040	0.094
Lung left blood	0.352	0.465	0.040	0.095
Lung left tissue	0.447	0.607	0.050	0.116
Lung right blood	0.352	0.482	0.041	0.095
Lung right tissue	0.467	0.639	0.052	0.123
Muscle head	0.372	0.504	0.041	0.101
Muscle trunk	0.370	0.508	0.042	0.098
Muscle arms	0.425	0.579	0.047	0.113
Muscle legs	0.508	0.692	0.059	0.137
Oesophagus	0.337	0.494	0.037	0.095
Pancreas	0.338	0.470	0.038	0.091
Skin head	0.424	0.562	0.047	0.121
Skin trunk	0.427	0.562	0.047	0.119
Skin arms	0.457	0.614	0.051	0.128
Skin legs	0.627	0.831	0.072	0.178
Skin Top Bottom Skin Layer	0.970	1.408	0.110	0.295
Small intestine wall	0.347	0.471	0.041	0.091
Small intestine contents	0.351	0.485	0.040	0.092
Spleen	0.340	0.464	0.039	0.089
Stomach wall	0.356	0.480	0.041	0.095
Stomach contents	0.343	0.470	0.039	0.090
Thymus	0.360	0.468	0.040	0.099
Thyroid	0.350	0.472	0.042	0.098
ovary left	0.347	0.463	0.030	0.100
ovary right	0.316	0.507	0.035	0.094
Uterus	0.356	0.485	0.040	0.094
Heart wall	0.337	0.467	0.039	0.087
Heart contents	0.351	0.480	0.039	0.092

Table 2. Absorbed dose in different organs of the ICRP110 male phantom for the natural radioactive series and for the ^{137}Cs uniformly distributed in the ground.

Organs/tissues	DCF(nGy h^{-1} per Bq kg^{-1})			
	^{238}U	^{232}Th	^{40}K	^{137}Cs
Adrenal left	0.410	0.438	0.037	0.081
Adrenal right	0.377	0.469	0.034	0.077
Gall bladder wall	0.397	0.475	0.043	0.087
Gall bladder contents	0.387	0.491	0.037	0.089
Urinary bladder wall	0.418	0.521	0.042	0.090
Urinary bladder contents	0.404	0.500	0.039	0.090
Brain	0.437	0.533	0.042	0.102
Breast left adipose tissue	0.518	0.575	0.053	0.113
Breast left glandular tissue	0.464	0.573	0.029	0.121
Breast right adipose tissue	0.471	0.592	0.042	0.112
Breast right glandular tissue	0.415	0.493	0.040	0.102
Ascending colon wall	0.398	0.482	0.036	0.088
Ascending colon contents	0.414	0.509	0.039	0.088
Transverse colon wall right	0.415	0.507	0.041	0.094
Transverse colon contents right	0.414	0.513	0.036	0.095
Transverse colon wall left	0.429	0.514	0.043	0.093
colon contents left	0.433	0.510	0.042	0.093
Descending colon wall	0.407	0.515	0.038	0.092
Descending colon contents	0.408	0.512	0.037	0.096
Sigmoid colon wall	0.404	0.483	0.040	0.085
Sigmoid colon contents	0.441	0.538	0.043	0.091
Kidney left cortex	0.389	0.485	0.037	0.087
Kidney left medulla	0.373	0.468	0.034	0.083
Kidney left pelvis	0.359	0.418	0.029	0.101
Kidney right cortex	0.396	0.483	0.037	0.089
Kidney right medulla	0.406	0.476	0.041	0.089
Kidney right pelvis	0.375	0.481	0.039	0.083
Liver	0.397	0.492	0.038	0.088
Lung left blood	0.392	0.479	0.040	0.085
Lung left tissue	0.492	0.604	0.049	0.111
Lung right blood	0.395	0.469	0.042	0.084
Lung right tissue	0.500	0.622	0.047	0.113
Muscle head	0.428	0.521	0.041	0.098
Muscle trunk	0.436	0.539	0.042	0.098
Muscle arms	0.504	0.616	0.048	0.116
Muscle legs	0.642	0.791	0.063	0.147
Oesophagus	0.376	0.443	0.038	0.087
Pancreas	0.379	0.460	0.036	0.078
Skin head	0.486	0.589	0.047	0.117
Skin trunk	0.499	0.595	0.048	0.117
Skin arms	0.536	0.641	0.051	0.126
Skin legs	0.751	0.908	0.073	0.182
Skin Top Bottom Skin Layer	1.262	1.519	0.116	0.303
Small intestine wall	0.390	0.490	0.037	0.085
Small intestine contents	0.395	0.491	0.038	0.088
Spleen	0.396	0.484	0.038	0.088
Stomach wall	0.395	0.487	0.038	0.086
Stomach contents	0.394	0.483	0.037	0.087
Thymus	0.395	0.505	0.040	0.089
Thyroid	0.375	0.461	0.033	0.087
Testis left	0.525	0.667	0.050	0.119
Testis right	0.534	0.683	0.056	0.113
Heart wall	0.373	0.467	0.036	0.085
Heart contents	0.388	0.486	0.037	0.088

Table 3. Averaged organ DCFs for male and female ICRP110 phantoms compared to the published values of the literature.

Organs	nSv h^{-1} per Bq kg^{-1}								
	^{238}U			^{232}Th			^{40}K		
	Zankl *et al.* (1997)	Sanusi *et al.* (2021)	This work	Zankl *et al.* (1997)	Sanusi *et al.* (2021)	This work	Zankl *et al.* (1997)	Sanusi *et al.* (2021)	This work
Adrenals	0.274	0.318	0.372	0.373	0.370	0.453	0.026	0.032	0.036
bladder	0.301	0.301	0.394	0.412	0.430	0.520	0.029	0.037	0.041
Brain	0.320	0.322	0.412	0.432	0.497	0.528	0.030	0.029	0.043
Breast	0.370	0.410	0.434	0.494	0.535	0.553	0.034	0.040	0.043
colon	0.291	0.353	0.384	0.396	0.512	0.501	0.028	0.034	0.040
Gonads	0.317	0.339	0.430	0.412	0.413	0.580	0.031	0.033	0.043
Kidneys	0.313	0.375	0.359	0.423	0.476	0.468	0.029	0.031	0.037
Liver	0.306	0.321	0.375	0.414	0.403	0.487	0.029	0.033	0.039
Lungs	0.329	0.346	0.425	0.443	0.445	0.546	0.031	0.033	0.045
Muscles	0.317	0.322	0.461	0.460	0.449	0.594	0.032	0.028	0.048
Oesophagus	0.282	0.313	0.357	0.384	0.386	0.468	0.027	0.030	0.037
Pancreas	0.279	0.312	0.359	0.379	0.404	0.465	0.028	0.031	0.037
Red bone marrow	0.305	0.339	0.244	0.411	0.456	0.303	0.029	0.033	0.024
Remainder tissues	0.300	0.326	0.376	0.412	0.456	0.478	0.029	0.030	0.039
Skeleton	0.358	0.422	0.441	0.479	0.470	0.590	0.032	0.034	0.047
Skin	0.394	0.448	0.526	0.522	0.565	0.663	0.036	0.041	0.055
Small intestine	0.288	0.302	0.371	0.394	0.446	0.484	0.027	0.034	0.039
Spleen	0.288	0.320	0.368	0.423	0.421	0.474	0.029	0.035	0.038
Stomach	0.300	0.338	0.372	0.406	0.471	0.480	0.029	0.036	0.039
Thymus	0.313	0.351	0.378	0.455	0.469	0.487	0.031	0.037	0.040
Thyroid	0.306	0.351	0.362	0.469	0.440	0.467	0.031	0.038	0.038

Table 4. Averaged organ DCFs for male and female ICRP110 phantoms for the ^{137}Cs radionuclide compared to published values by Sanusi *et al.* (2021).

Organs	nSv h^{-1} per Bq kg^{-1}	
	Sanusi *et al.*	This work
Adrenals	0.063	0.077
bladder	0.061	0.096
Brain	0.051	0.102
Breast	0.078	0.110
colon	0.060	0.092
Gonads	0.066	0.107
Kidneys	0.068	0.087
Liver	0.065	0.091
Lungs	0.070	0.103
Muscles	0.059	0.114
Oesophagus	0.064	0.091
Pancreas	0.060	0.084
Red bone marrow	0.065	0.050
Remainder tissues	0.064	0.090
Skeleton	0.068	0.120
Skin	0.081	0.136
Small intestine	0.070	0.089
Spleen	0.067	0.088
Stomach	0.064	0.090
Thymus	0.070	0.094
Thyroid	0.073	0.092

^{137}Cs, the comparison with Sanusi *et al.* (2021) in Table 4 shows discrepancies due to different physical approximations. Sanusi *et al.*'s method, which simplifies secondary electron energy deposition, likely underestimates absorbed doses in shielded organs. This effect is enhanced at energies of the same order of magnitude as the ^{137}Cs emission energy (662 keV).

Table 5 shows the results of the present work compared to the results obtained indirectly from the ICRP 144 calculations using fitted DCF curves constructed from the planar source results at four depths and a numerical integration procedure. The data used is available via supplementary material to this report (ICRP, 2020). The accuracy of the calculation method integrating the ICRP 144 data is estimated at 10% as the available data is limited to four soil depths less than 20 cm, so our fitting and integration was performed up to a source thickness of 50 cm. Despite these limitations, good agreement is achieved between the two methods. Our DCFs values are higher than those indirectly derived from ICRP 144 data. This discrepancy is to be expected since we performed our calculation using volumetric source for soil depth up to 2 m.

The discrepancy between the results of the present work and the published ones using mathematical phantoms, expressed in percent of the published value of the organ-absorbed dose, is presented in Figures 3 and 4. The complexity of the biological human tissues is accurately represented by unit voxels rather than by mathematical forms, which lead to a loss of information at low scales. The optimised geometry and efficient particle transport algorithm used in this study resulted

Table 5. Averaged organ DCFs for male and female ICRP110 phantoms compared to values obtained from published ICRP 144 report data using the same phantom type (ICRP, 2020).

Organs	^{238}U		^{232}Th		^{40}K	
	ICRP 144	This work	ICRP 144	This work	ICRP 144	This work
Adrenals	0.346	0.372	0.426	0.453	0.032	0.036
Brain	0.347	0.412	0.428	0.528	0.036	0.043
Breast	0.366	0.434	0.448	0.553	0.040	0.043
Colon	0.401	0.384	0.503	0.501	0.039	0.040
Gonads	0.368	0.430	0.449	0.580	0.038	0.043
Kidneys	0.338	0.359	0.416	0.468	0.033	0.037
Liver	0.342	0.375	0.420	0.487	0.036	0.039
Lungs	0.364	0.425	0.444	0.546	0.039	0.045
Muscles	0.423	0.461	0.516	0.594	0.040	0.048
Oesophagus	0.264	0.357	0.300	0.468	0.033	0.037
Pancreas	0.324	0.359	0.401	0.465	0.031	0.037
Red bone marrow	0.238	0.244	0.300	0.303	0.029	0.024
Skin	0.482	0.526	0.469	0.663	0.049	0.055
Spleen	0.324	0.368	0.399	0.474	0.032	0.038
Thymus	0.352	0.378	0.432	0.487	0.036	0.040
Thyroid	0.359	0.362	0.451	0.467	0.033	0.038

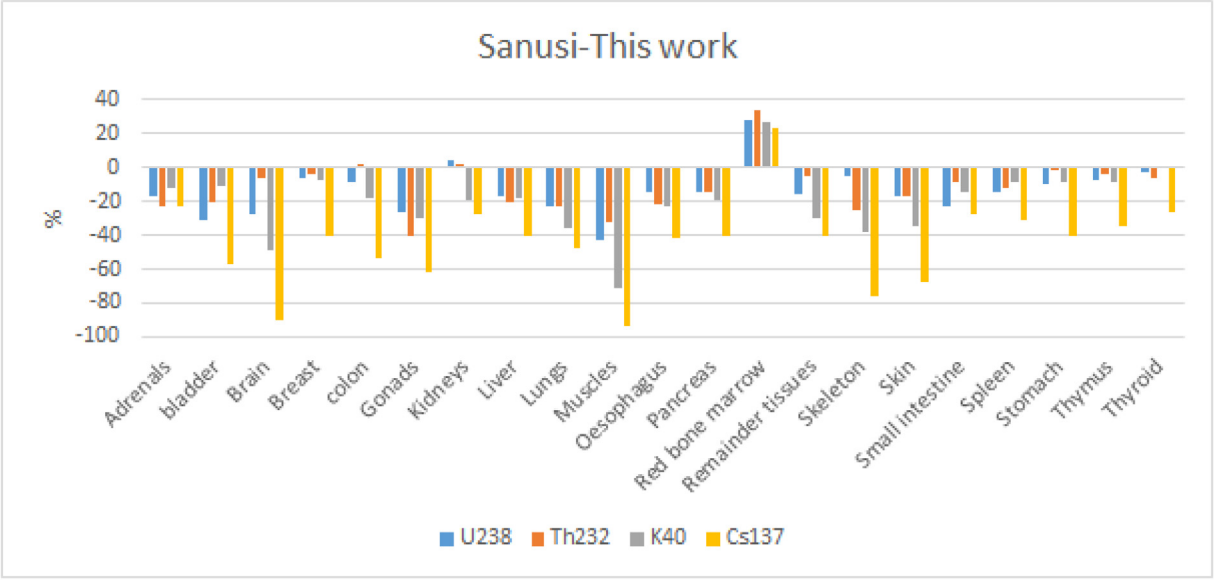

Fig. 3. Discrepancy between the DCFs values of the present work and those from (Sanusi *et al.*, 2021).

in a significant computation time gain, eliminating the need for physical approximations such as locally killing the secondary particles, reducing the entire gamma ray spectrum or minimising the soil and air volume dimensions (Sanusi *et al.*, 2021; Zankl *et al.*, 1997).

Table 6 compares the effective dose derived from organ DCFs in our study with literature values. Although the discrepancy in organ DCFs between the present work and the literature is relatively large, the values of the effective doses are close to each other. This is because the organ tissue factors w_T used in equation (2) for calculating the effective dose are very low weighting factors. This leads to the conclusion that investigation on more detailed dose assessment is necessary.

4 Conclusion

We performed a two-stage Monte Carlo simulation using Geant4 to calculate dose-to-organ conversion factors (DCFs) for external gamma radiation exposure from ground-distributed radioactive sources. Voxel-based ICRP110 female and male phantoms and an optimised soil-air geometry were used to realistically transport particles and save computing time without physical approximations. We determined DCFs for the ^{238}U and ^{232}Th series, and the radionuclides ^{40}K and ^{137}Cs, and tabulated results for 55 female and 54 male organs. Our results are higher than published values using less accurate MIRD phantoms. The results indirectly obtained

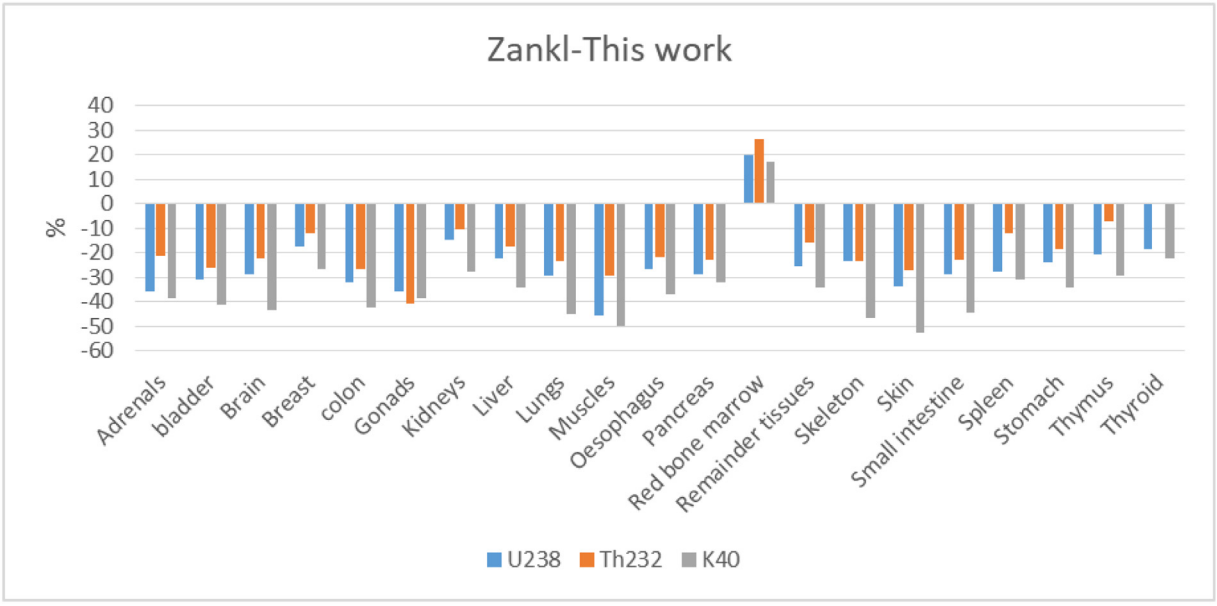

Fig. 4. Discrepancy between the DCFs values of the present work and those from (Zankl *et al.*, 1997).

Table 6. Effective dose conversion factors from the present work compared to the literature values.

Reference	Effective dose conversion factor (nSv h^{-1} per Bq kg^{-1})			
	^{238}U	^{232}Th	^{40}K	^{137}Cs
Zankl *et al.* (1997)	0.311	0.419	0.030	–
Clouvas *et al.* (2000)	0.279	0.381	0.028	0.087
Krstic and Nikezic (2009)	–	–	–	0.042
Petoussi-Henss *et al.* (1991)	0.319	0.446	0.030	–
a Askri *et al.* (2023)	0.287	0.419	0.028	0.070
b Askri *et al.* (2023)	0.332	0.469	0.032	0.088
Malins *et al.* (2015)	0.311	0.414	0.029	–
Sanusi *et al.* (2021)	0.349	0.465	0.034	0.067
The present Work	0.375	0.485	0.038	0.091

[a] Numerical solution of the Boltzmann transport equation.
[b] Monte Carlo simulation using Geant4 code.

from to the data provided by the ICRP 144 report using the same voxel phantoms are in good agreement with the present work. Despite discrepancies in organ DCFs, effective dose estimates for human exposure to soil radioactivity agree with literature values, highlighting the need for further detailed research on organ absorbed DCFs. This study is the initial step in a broader program aimed at enhancing predictions of human exposure to contaminated soils from radioactive waste. Future work includes benchmarking simulation exercises to test the model under various scenarios.

Funding

This research did not receive any specific funding.

Conflicts of interest

The authors declare that they have no conflict of interest.

Data availability statement

The authors confirm that the data supporting the findings of this study are available within the article.

References

Agostinelli S, Allison J, Amako K, *et al.* 2003. Geant4 a simulation toolkit. *Nucl. Instrum. Methods Phys. Res. A* 506: 250–303.

Allison J, Amako K, Apostolakis J *et al.* 2016. Recent developments in Geant4. *Nucl. Instrum. Methods Phys. Res. A* 835: 186–225.

Askri B, Manai K, Bouzouita A, *et al.* 2023. Estimation of the gamma-ray field in air from radioactive sources in the ground by numerical solution of the Boltzmann transport equation. *Radiat. Protect. Dosim.* 199: 631–645.

Askri B. 2016. Monte Carlo method for determining the response of portable gamma detector for in situ measurement of terrestrial gamma ray field. *Nucl. Sci. Technol.* 27: 81.

Askri B. 2015. Application of optimised geometry for the Monte Carlo simulation of a gamma-ray field in air created by sources distributed in the ground. *Radiat. Meas*. 72: 1–11.
Askri B, Manai K, Trabelsi A, *et al.* 2008. Optimised geometry to calculate dose rate conversion coefficient for external exposure to photons. *Radiat. Protect. Dosim*. 128: 279–288.
Clouvas A, Xanthos S, Domis-Antonopoulos M, *et al.* 2000. Monte Carlo calculation of dose rate conversion factors. *Health Phys*. 78: 295–302.
Eckerman KF, Ryman JC. 1993. External Exposure to Radionuclides in Air, Water, and Soil. Federal Guidance Report No. 12. United States of Environmental Protection Agency, Washington DC.
ICRP. 1991. 1990 Recommendations of the International Commission on Radiological Protection. ICRP Publication 60. *Ann. ICRP* 21: 1–201.
ICRP. 1995. Basic Anatomical & Physiological Data for use in Radiological Protection – The Skeleton. ICRP Publication 70. *Ann. ICRP* 25: 1–80.
ICRP. 2002. Basic Anatomical and Physiological Data for Use in Radiological Protection Reference Values. ICRP Publication 89. *Ann. ICRP* 32: 1–277.
ICRP. 2007. The 2007 Recommendations of the International Commission on Radiological Protection. ICRP Publication 103. *Ann. ICRP* 37: 1–332.
ICRP. 2009. Adult reference computational phantoms, ICRP Publ. 110. *Ann. ICRP* 39: 1–166.
ICRP. 2010. Conversion Coefficients for Radiological Protection Quantities for External Radiation Exposures. ICRP Publication 116, *Ann. ICRP* 40: 1–257.
ICRP. 2020. Dose Coefficients for External Exposures to Environmental Sources. ICRP Publication 144, *Ann. ICRP* 49: 11–145.
Incerti S, Brown J, Guatelli S. 2020. Advances in Geant4 applications in medicine. *Phys. Med*. 70: 224–227.
Jacob P, Paretzke HG, Rosenbaum H, *et al.* 1986. Effective dose equivalents for photon exposures from plane sources on the ground. *Radiat. Protect. Dosim*. 14: 299–310.
Johnson JR, Dunford DW. 1985. Comparison of the ICRP and MIRD models for Fe metabolism in man. *Health Phys*. 49: 211–219.
Krstic D, Nikezic D. 2009. External doses to humans from ^{137}Cs in soil. *Health Phys*. 91: 249–257.
Kramer R, Zankl M, Williams G, Drexler G. 1982. The calculation of dose from external photon exposures using reference human phantoms and Monte Carlo methods: Part I. The male (Adam) and female (Eva) adult mathematical phantoms. GSF-Bericht S-885. Neuherberg: GSF—National Research Center for Environment and Health.
Malins A, Machida M, Saito K, *et al.* 2015. Comment on 'Update of ^{40}K and ^{226}Ra and ^{232}Th series γ-to-dose conversion factors for soil'. *J. Environ. Radioact*. 144: 179–180.
Portugal M, Baptista M, Vaz P, *et al.* 2022. Patients' organ dose and risk assessment in interventional cardiology procedures. *Radiat. Phys. Chem*. 198: 110253.
Petoussi-Henss N, Jacob P, Zankl M, *et al.* 1991. Organ doses for foetuses, babies, children and adults from environmental gamma rays. *Radiat. Protect. Dosim*. 37: 31–41.
Rezaeian P, Khandan LT, Torabi H, *et al.* 2022. Fabrication of head phantom to investigate the effect of heterogeneity on the absorbed dose in radiotherapy. *Iran J Sci Technol Trans Sci* 46: 1295–1300.
Saito K, Moriuchi S. 1985. Development of a Monte Carlo code for the calculation of gamma ray transport in the natural environment. *Radiat. Protect. Dosim*. 12: 21–28.
Saito K, Jacob P. 1995. Gamma ray field in the air due to sources in the ground. *Radiat. Protect. Dosim*. 58: 29–45.
Saito K. 1991. External dose due to terrestrial gamma rays on the snow cover. *Radiat. Protect. Dosim*. 35: 31–39.
Sanusi MSM, Hassan WMSW, Hashim S, *et al.* 2021. Tabulation of organ dose conversion factors for terrestrial radioactivity monitoring program. *Appl. Radiat. Isot*. 109791.
Snyder WS, Ford MR, Warner GG. 1978. Estimates of specific absorbed fractions for monoenergetic photon sources uniformly distributed in various organs of a heterogeneous phantom MIRD Pamphlet 5, revised. New York: Society of Nuclear Medicine.
Xu X, Xiao-Min Z, Jing N, *et al.* 2023. Study on the ^{24}Na specific activity induced by external neutron irradiation based on ICRP 110 computational phantoms. *Appl. Radiat. Isot*. 195: 110735.
Zankl M, Petoussi-Henss N, Drexler G, *et al.* 1997. The Calculation of Dose from External Photon Exposures Using Reference Human Phantoms and Monte Carlo Methods Part VII: Organ Doses Due to Parallel and Environmental Exposure Geometries. GSF-Berich.

Cite this article as: Bouzouita A, Askri B, Manai K, Trabelsi A. 2024. Voxel-based Monte Carlo simulation of human external exposure to terrestrial gamma radiation. *Radioprotection* 59(4): 296–305